2017

Structure Evolution and Multiferroic Properties in Cobalt Doped $Bi_4NdTi_3Fe_{1-x}Co_xO_{15}$-$Bi_3NdTi_2Fe_{1-x}CoxO_{12-\delta}$ Intergrowth Aurivillius Compounds

D. L. Zhang
University of Science and Technology of China

W. C. Huang
University of Science and Technology of China, Hefei

Z. W. Chen
University of Science and Technology of China

W. B. Zhao
University of Science and Technology of China

L. Feng
University of Science and Technology of China

See next page for additional authors

SCIENTIFIC REPORTS

OPEN

Received: 08 September 2016
Accepted: 27 January 2017
Published: 08 March 2017

Structure Evolution and Multiferroic Properties in Cobalt Doped $Bi_4NdTi_3Fe_{1-x}Co_xO_{15}$-$Bi_3NdTi_2Fe_{1-x}Co_xO_{12-\delta}$ Intergrowth Aurivillius Compounds

D. L. Zhang[1], W. C. Huang[1], Z. W. Chen[1], W. B. Zhao[1], L. Feng[1], M. Li[1], Y. W. Yin[1,2], S. N. Dong[1] & X. G. Li[1,3,4]

Here, we report the structure evolution, magnetic and ferroelectric properties in Co-doped 4- and 3-layered intergrowth Aurivillius compounds $Bi_4NdTi_3Fe_{1-x}Co_xO_{15}$-$Bi_3NdTi_2Fe_{1-x}Co_xO_{12-\delta}$. The compounds suffer a structure evolution from the parent 4-layered phase ($Bi_4NdTi_3FeO_{15}$) to 3-layered phase ($Bi_3NdTi_2CoO_{12-\delta}$) with increasing cobalt doping level from 0 to 1. Meanwhile the remanent magnetization and polarization show opposite variation tendencies against the doping level, and the sample with $x = 0.3$ has the largest remanent magnetization and the smallest polarization. It is believed that the Co concentration dependent magnetic properties are related to the population of the Fe^{3+} -O-Co^{3+} bonds, while the suppressed ferroelectric polarization is due to the enhanced leakage current caused by the increasing Co concentration. Furthermore, the samples ($x = 0.1$–0.7) with ferromagnetism show magnetoelectric coupling effects at room temperature. The results indicate that it is an effective method to create new multiferroic materials through modifying natural superlattices.

The search for multiferroic materials combining electric and magnetic properties in a single phase has attracted a lot of attention in the perspective of future spintronic or magnetoelectronic devices[1–3]. Unfortunately, only a handful of single phase multiferroics have been discovered so far, and most of them are not suitable for practical applications at present, either because the room temperature polarization/magnetization is too small or their mutual coupling is too weak[4–6]. Therefore people are still hunting for new multiferroic systems[2,7]. One possible route for designing single-phase multiferroic materials is to start from a series of well-established ferroelectrics and create additional functionality by incorporating magnetic ions into these systems[1,8,9]. A promising class of materials for this purpose is the so-called Aurivillius phases with a naturally layered perovskite-related crystal structure, which consists of n perovskite-like layers $(A_{n-1}B_nO_{3n+1})^{2-}$, stacked along the [001] direction, and separated by fluorite-like $(Bi_2O_2)^{2+}$ layers[10]. The overall chemical composition is thus $Bi_2A_{n-1}B_nO_{3n+3}$, where many different cations can be incorporated on the A and B sites within the perovskite-like layers[11]. The series of Aurivillius phase compounds are well known for their excellent ferroelectric properties with very low fatigue[12], and offer great potential for tailoring specific properties by varying different ionic compositions or even number of layers[8,13,14]. By doping with magnetic cations, the bismuth-based Aurivillius phase compounds were found to have a room temperature ferromagnetic order besides the natural ferroelectricity, indicating their multiferroic potential[8,9,15–17]. Moreover, the Sm and Co co-doped 3-layered ($n = 3$) $Bi_{4-x}Sm_xTi_{3-x}Co_xO_{12-\delta}$ ($0 \leq x \leq 0.07$) ceramics show a magnetoelectric (ME) coupling coefficient of 0.65 mV/cm·Oe at room temperature[15], while the 5-layered ($n = 5$) $SrBi_5Fe_{0.5}Co_{0.5}Ti_5O_{18}$ ceramic was found to show a ME coupling coefficient of 0.27 mV/cm·Oe[8]. Thus this kind of material is one of the excellent choices for ME applications and deserves further investigation.

[1]Hefei National Laboratory for Physical Sciences at the Microscale, Department of Physics, University of Science and Technology of China, Hefei 230026, China. [2]Department of Physics and Astronomy, University of Nebraska, Lincoln, NE 68588, USA. [3]Key Laboratory of Materials Physics, Institute of Solid State Physics, CAS, Hefei 230026, China. [4]Collaborative Innovation Center of Advanced Microstructures, Nanjing 210093, China. Correspondence and requests for materials should be addressed to Y.W.Y. (email: yyin11@unl.edu) or X.G.L. (email: lixg@ustc.edu.cn)

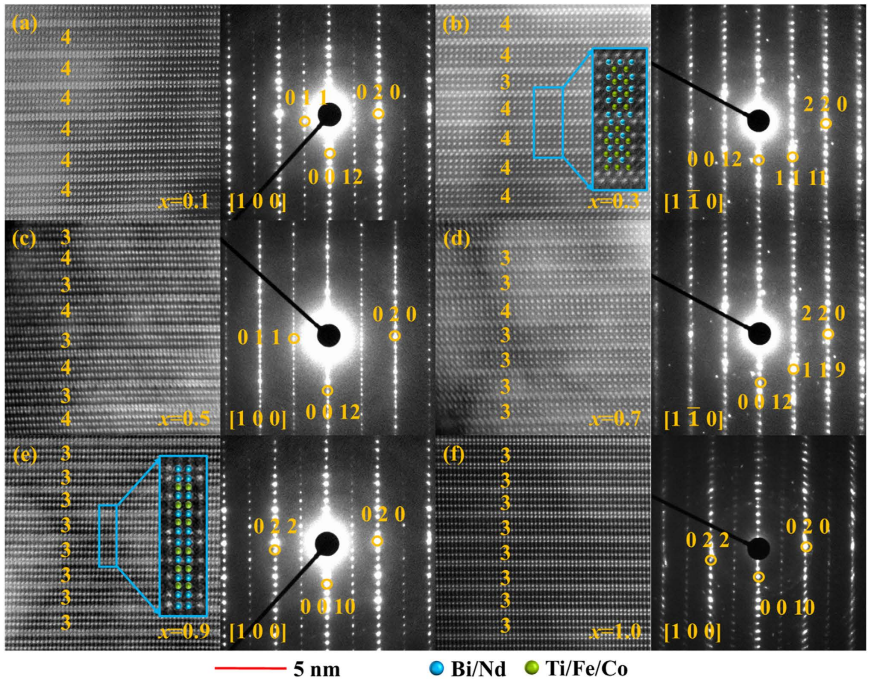

Figure 1. HAADF images and SAED patterns of BNTFC–x: (**a**) $x = 0.1$; (**b**) $x = 0.3$; (**c**) $x = 0.5$; (**d**) $x = 0.7$; (**e**) $x = 0.9$; (**f**) $x = 1.0$. The big white spots represent the Bi (Nd) atoms, while the small spots located near the center of Bi/Nd lattice represent the Ti/Fe/Co atoms. The inset in (**b**) and (**e**) is a magnifying image for 4- and 3-layered phase, respectively, where the azury and green sphere denote Bi/Nd and Ti/Fe/Co atoms, respectively. For (**a**,**c**,**e** and **f**), the viewing direction is along [100], while for (**b**) and (**c**) the viewing direction is along $[\bar{1}10]$. For $x \leq 0.5$, the marked diffraction spots belong to 4-layered phase, while for $x > 0.5$ the marked diffraction spots belong to 3-layered phase.

Furthermore, due to the complexity of the structure, an interesting phenomenon called intergrowth has been reported in Aurivillius compounds[18–20]. It has been demonstrated that the ferroelectricity of 4- and 3-layered intergrowth compounds is larger than that of individual 4- or 3-layered compound[21,22]. However, the effects of magnetic ions doping on ferroelectric, magnetic and multiferroic properties are still unknown in such an intergrowth superlattice system.

Here we successfully synthesized a series of $Bi_4NdTi_3Fe_{1-x}Co_xO_{15}$-$Bi_3NdTi_2Fe_{1-x}Co_xO_{12-\delta}$ (BNTFC-x) compounds with different ratios of 4- and 3-layered Aurivillius intergrowth superlattice structure. It was found that as the cobalt doping concentration increases from 0 to 1, the samples suffer a structure evolution from 4-layers to 3-layers. The observed magnetic and ferroelectric properties can be well explained by the magnetic ions doping and the intergrowth structure evolution.

Results and Discussion

To clarify the structure evolution of the $Bi_4NdTi_3Fe_{1-x}Co_xO_{15}$-$Bi_3NdTi_2Fe_{1-x}Co_xO_{12-\delta}$ (BNTFC-x) compounds, the high-angle annular dark-field (HAADF) images and selected area electron diffraction (SAED) were performed, as shown in Fig. 1. In the HAADF images, the big bright spots stand for the location of the Bi/Nd atoms while the small spots located near the center of Bi/Nd lattice represent the Ti/Fe/Co atoms as depicted in the inset of Fig. 1(b) (4-layered) and (e) (3-layered). It can be seen that the fluorite-like $(Bi_2O_2)^{2+}$ layers and peroskite-like $(A_{n-1}B_nO_{3n+1})^{2-}$ layers are stacking along c direction, indicating that all compounds have a typical Aurivillius layered structure. From the SAED patterns, the electron incidence direction, namely the view direction, can be obtained, as marked in Fig. 1. As shown in Fig. 1(a), the 4-layered lattice can be clearly distinguished for $x = 0.1$. As the Co concentration increases to 0.3, the 3-layered lattice begins to appear as shown in Fig. 1(b). While x increases to 0.5, the 4-layered and 3-layered structures alternately stack along the [001] direction (shown in Fig. 1(c)). With the x further increasing to 0.7, the 3-layered structure starts to dominate (shown in Fig. 1(d)), and at last for $x = 0.9$ and 1 components, the 4-layered Aurivillius structure almost disappears (shown in Fig. 1(e) and (f)). The HAADF results indicate that increasing Co doping level makes the BNTFC-x compound experiencing a structure evolution from 4-layered structure to 3-layered structure. This intergrowth phenomenon has also been reported in $Sr_xBi_{7-x}Fe_{1.5}Co_{1.5}Ti_3O_{21-\delta}$, which undergoes a phase evolution from 6-layers to 4-layers when the concentration of A-site doped strontium increases from 0 to 1[14].

The room temperature powder X-ray diffraction (XRD) patterns with data refined by Rietveld Method *via* Materials Analysis Using Diffraction (MAUD) program[23,24] for BNTFC-x ceramics are shown in Fig. 2. Quantitative analysis confirms that three phases, including 4-layered phase $Bi_4NdTi_3Fe_{1-x}Co_xO_{15}$ ($n = 4$), 3-layered phase $Bi_3NdTi_2Fe_{1-x}Co_xO_{12-\delta}$ ($n = 3$), and an impurity phase $Bi_{12}TiO_{20}$ coexist in the BNTFC-x system. The refinements were based on space group $A2_1am$ (No. 36) for 4-layered phase[25], B2cb (No. 41) for 3-layered

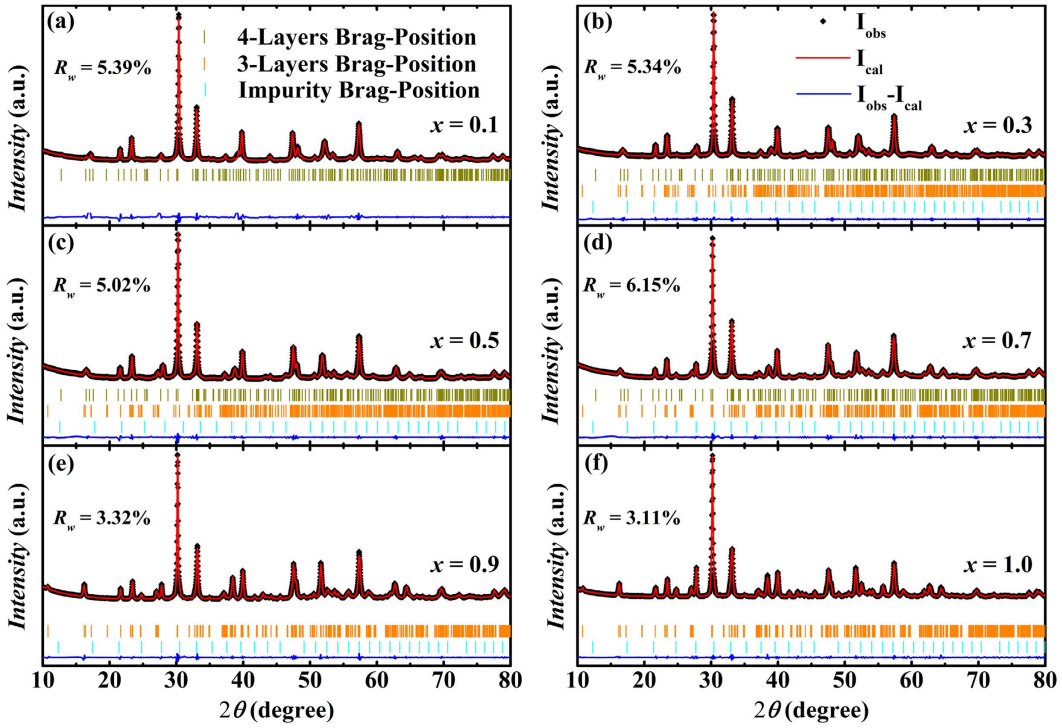

Figure 2. XRD patterns and refined results of BNTFC-*x* samples with (**a**) $x = 0.1$; (**b**) $x = 0.3$; (**c**) $x = 0.5$; (**d**) $x = 0.7$; (**e**) $x = 0.9$; (**f**) $x = 1.0$.

phase[26] and I23 (No. 197) for $Bi_{12}TiO_{20}$ phase[27]. The good matching between experimental and calculated XRD patterns is demonstrated by the low R_w value for all compounds ($R_w \leq 6.15\%$), as shown in Fig. 2. To better understand and analysis the structures, the schematic structure diagrams of 4- and 3-layered phases are shown in Fig. 3(a) and (b), respectively. The Ti, Fe and Co cations were set to occupy the same position (B site in the center of each perovskite structure in the perovskite-like layer) with fixed Ti occupancy (3/4 in 4-layer phase, and 2/3 in 3-layer phase) and changeable occupancies of Fe and Co with the cobalt nominal doping level ((1-*x*)/4 for Fe and *x*/4 for Co in 4-layer phase, (1-*x*)/3 for Fe and *x*/3 for Co in 3-layer phase).

The lattice parameters *a* and *b* obtained by refinement gradually decrease and *c* increases in both 4-layered (Fig. 4(a)) and 3-layered (Fig. 4(b)) phase with increasing cobalt concentration. As shown in Fig. 4(c), the volume fraction of 4- (3-) layered phase gradually decreases (increases) from 100% (0) to 0 (85.34%) as *x* increases from 0 to 1, also confirming that the samples suffer a structure evolution from 4-layered phase to 3-layered phase. The fraction of the $Bi_{12}TiO_{20}$ phase increases with the Co concentration in the samples with $x < 0.5$, and keeps at about 15% for $x \geq 0.5$. The impurity phase ($Bi_{12}TiO_{20}$) is induced by the element loss during the structure evolution process, similar to the situation in $Sr_xBi_{7-x}Fe_{1.5}Co_{1.5}Ti_3O_{21-\delta}$ system[14]. According to the results of XRD patterns and HAADF images, the BNTFC-*x* compounds undergo a structure evolution with a two-phase modulated superlattice when the concentration of Co changes. In other words, the micro superlattice structure can be naturally controlled by the cobalt doping level.

In addition, the Fe/Co ions can occupy two non-equivalent positions (center of inner and outer octahedrons between two $(Bi_2O_2)^{2+}$ layers) in 4- and 3-layered structures. In 4-layered $Bi_5Ti_3FeO_{15}$, these octahedrally coordinated center sites are shared between Ti^{4+} and Fe^{3+} cations, and a quasi-random cation distribution is observed in experiments[25,28]. Similarly, it can be assumed that Ti^{4+}, Fe^{3+}, and Co^{3+} cations are randomly distributed in the octahedral center positions in both 4- and 3-layered structures. In perovskite-like compounds the most probable valence states of Fe and Co are + 3. According to Goodenough-Kanamori rules[9,29–31], Fe^{3+} -O-Fe^{3+} and Co^{3+} -O-Co^{3+} superexchange interactions with the nature of antiferromagnetism exist in $x = 0$ and 1 samples, respectively, making the ground state of these two compounds to be antiferromagnetic. Based on the discussions on the occupations and interactions of Fe/Co cations, it can be expected that the structure evolution of BNTFC-*x* will have a significant impact on the physical properties, *e.g.* magnetism and ferroelectricity. To verify this, we systemically measured the magnetic and ferroelectric properties of BNTFC-*x* compounds, and discussed the relationship between the structure and properties as follows.

The room temperature magnetic hysteresis loops for BNTFC-*x* are shown in Fig. 5(a). The magnetization (*M*) *versus* applied field (*H*) curves of $x = 0.1$ to 0.7 samples show a typical ferromagnetic hysteresis feature, while those for $x = 0$, 0.9 and 1.0 show a linear behavior. The remanent magnetization (M_r) and saturation magnetization (M_s, obtained from the *M*-*H* curves after deducting the linear part) gradually increase and reach a maximum with increasing Co content to $x = 0.3$, and then decreases with further increasing Co content, as shown in Fig. 5(b). It is known that the ground state of $Bi_4NdTi_3FeO_{15}$ ($x = 0$) is antiferromagnetic. When Co^{3+} replaces parts of Fe^{3+} cations, some Fe^{3+} -O-Fe^{3+} chains will be destroyed, while the antiparallel Fe^{3+} and Co^{3+} superexchange

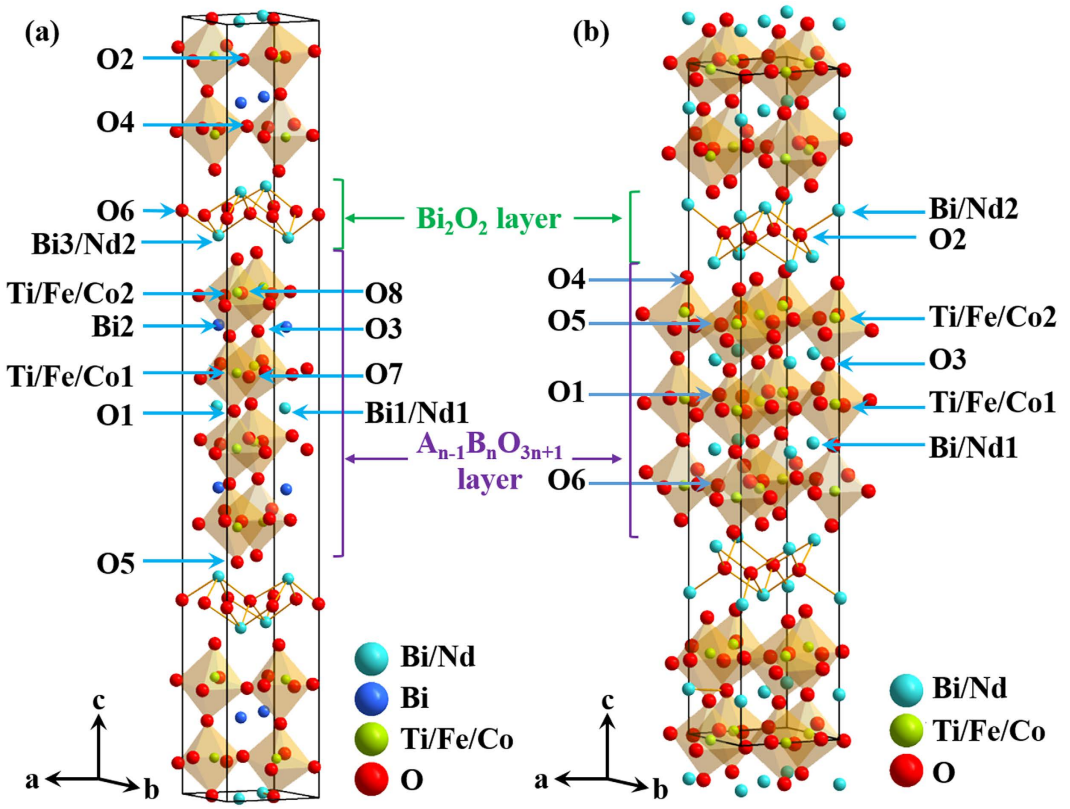

Figure 3. Schematic structure diagram of (**a**) 4- and (**b**) 3-layered phases, with atom positions marked in the figure.

interaction appears. Considering the difference of magnetic moments between a single Fe^{3+} (5.916 μ_B) and a single Co^{3+} (4.899 μ_B)[32], the interaction of Fe^{3+} -O-Co^{3+} should contribute to a net magnetization, as discussed in $Bi_5Fe_{0.5}Co_{0.5}Ti_3O_{15}$[33] and $Bi_4NdFe_{0.5}Co_{0.5}Ti_3O_{15}$[16] ceramics. In the situation of $x = 0.1$, namely 10% Fe^{3+} ions are substituted by Co^{3+}, the formation of Fe^{3+} -O-Co^{3+} bonds results in the appearance of ferromagnetism. In $x = 0.3$, more Fe^{3+} -O-Co^{3+} bonds form, leading to a larger remanent magnetization. While for $x > 0.5$, the decrease of the amount of Fe^{3+} -O-Co^{3+} bonds may lead to the diminution of magnetization. As for $x = 0.9$, the concentration of Fe^{3+} ions is too low to construct effective Fe^{3+} -O-Co^{3+} order, the system may be antiferromagnetic or paramagnetic at room temperature, just like $Bi_5Ti_3FeO_{15}$[34]. Thus, it can be proposed that the magnetization of BNTFC-x may be mainly contributed by the population of Fe^{3+} -O-Co^{3+} local structure due to the cobalt doping[33]. Besides, the Ti/Fe/Co-O-Ti/Fe/Co angles may be affected by Co substitution[35] and structure evolution[22], which could also affect the observed magnetic properties. It should be noted that the most prominent remanent magnetization ($M_r = 123$ memu/g) at $x = 0.3$ is about 31 times larger than that of $Bi_5Ti_3Fe_{0.5}Co_{0.5}O_{15}$ (3.9 memu/g)[33], and comparable with that of $Bi_4NdTi_3Fe_{0.5}Co_{0.5}O_{15}$ (165 memu/g)[16] and $Bi_4NdTi_3Fe_{0.7}Ni_{0.3}O_{15}$ (194 memu/g)[36].

It has been reported that the doping of an Aurivillius phase with cobalt will lead to the generation of magnetic second-phase inclusions (Co/Fe-rich spinel phases) which volume fraction is too small to be visible in XRD but may be already enough to contribute significant ferromagnetic signal[9,37,38]. Generally, the Fe and Co-rich magnetic inclusions have a chemical formula $Fe_{3-y}Co_yO_4$ ($0 \leq y \leq 3$), and the remanent magnetizations (0–20 emu/g) at room temperature decrease with increasing Co content[39–44]. Following the effective statistical method proposed by M. Schmidt *et al.*[38], the volume fraction of the possible inclusions and their upper limit impact on magnetic contributions (M_i/M_r, where M_i is the remanent magnetization of the inclusions and M_r is that of the specimen) for the worst case scenario were carefully estimated *via* energy selective backscatter (ESB) image and energy dispersive X-ray analysis (EDX). For the samples with ferromagnetic signals, namely, $x = 0.1$, 0.3, 0.5, and 0.7, the magnetic contributions to the corresponding specimens of the inclusions are conservatively estimated to be about or smaller than 3.9%, 1.9%, 3.8%, and 1.5%, respectively. While for $x = 0.9$ and 1.0, the inclusions are paramagnetic at 300 K[44,45], and have no magnetic contributions to the main phase. Based on the criteria of the comprehensive framework raised by M. Schmidt *et al.*[38], we believe that the magnetic results do reflect the intrinsic ferromagnetic properties of the main phase. Detailed calculations are presented in Part I of the Supplementary Material.

Figure 6 shows the room temperature polarization (P) *versus* electric field (E) curves of BNTFC-x samples, indicating that all specimen have a good ferroelectricity. With increasing the cobalt doping concentration, the remanent polarization P_r first decreases and reaches the minimum (4.26 $\mu C/cm^2$) at $x = 0.3$, and then gradually increases with further doping. The obtained P_r for BNTFC-x is better than $Bi_4NdTi_3Fe_{0.5}Co_{0.5}O_{15}$ (1 $\mu C/cm^2$)[16]

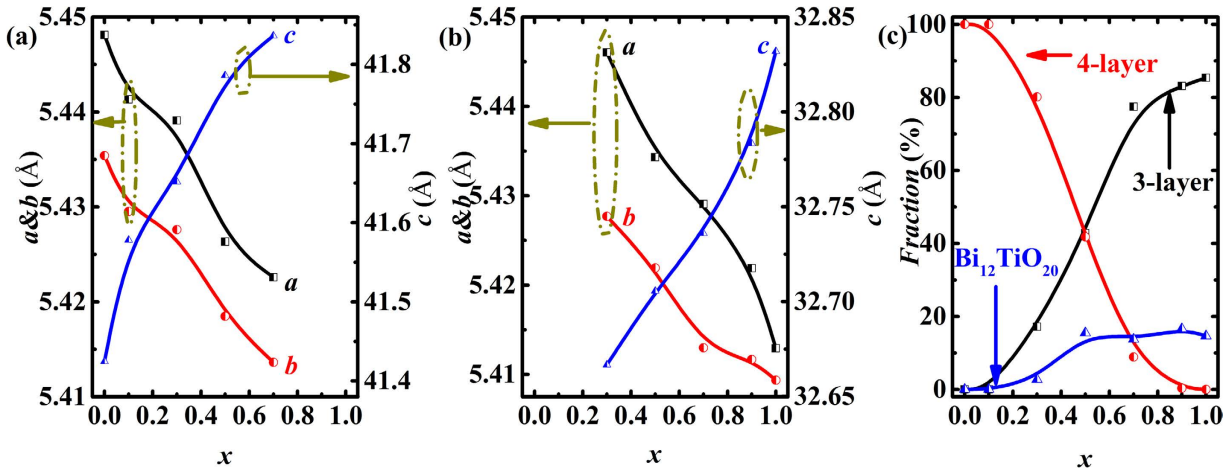

Figure 4. Lattice parameters of (**a**) 4-layered phase and (**b**) 3-layered phase; (**c**) the volume fraction of 4-, 3-layered and impurity ($Bi_{12}TiO_{20}$) phases.

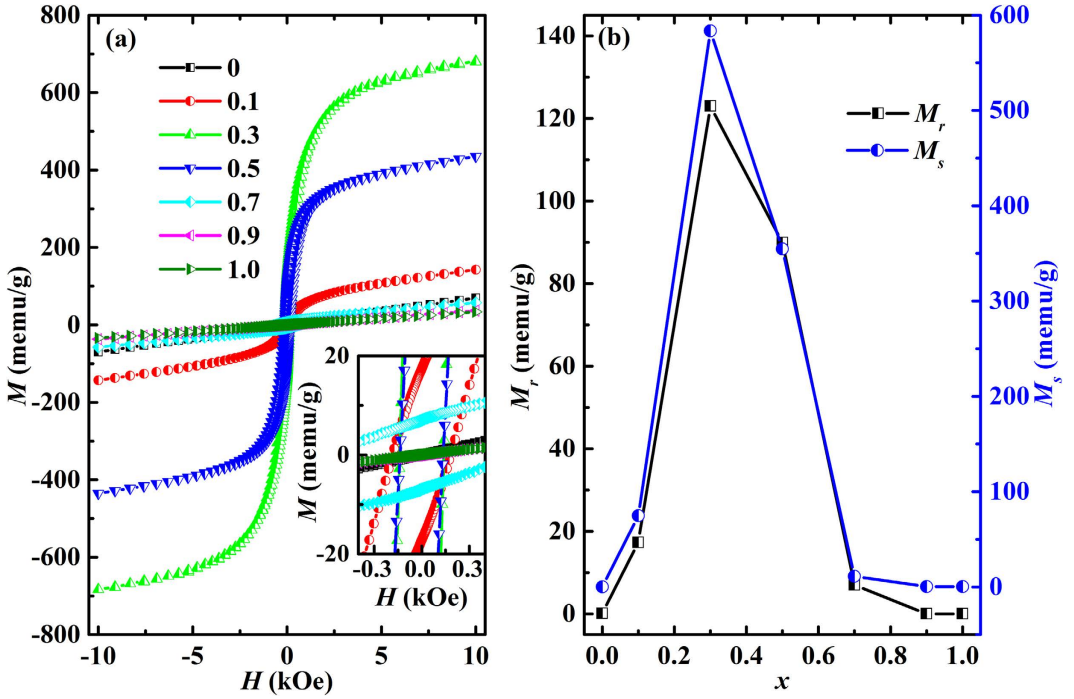

Figure 5. (**a**) Room temperature *M-H* hysteresis loops. Inset is the zoom of the main plot; (**b**) M_r and M_s as a function of cobalt doping level *x* for BNTFC-*x* ($x = 0$, 0.1, 0.3, 0.5, 0.7, 0.9 and 1).

as well as $Bi_4NdTi_3Fe_{0.7}Ni_{0.3}O_{15}$ (4.3 μC/cm^2)[36], and comparable to that of $Bi_5Ti_3Fe_{0.5}Co_{0.5}O_{15}$ ceramics (6.5 μC/cm^2)[33]. While the coercive field E_c of BNTFC-*x* keeps decreasing as the cobalt concentration increases, which should be related to the smaller coercive field in 3-layered phase than 4-layered phase[21]. It should be noted that the P_r-*x* curve (Fig. 6(b), black line) shows an opposite variation tendency as compared with M_r-*x* curve (Fig. 5(b), black line), indicating a correlation between ferroelectricity and magnetism. For example, the minimum P_r and maximum M_r are observed in $x = 0.3$ sample. The P_r-*x* curve indicates that the P_r values of the 4- and 3- layered intergrowth compounds ($0.1 < x < 0.9$) are smaller than that of individual 4- ($x = 0$) or 3- ($x = 1$) layered compound, which is opposite to previous reports (no magnetic ions doped in the samples)[21,22], probably due to the magnetic ion doping in our system. Figure 6(b) (red line) shows the resistivity (ρ) for the BNTFC-*x* at room temperature. The similar variation tendency of P_r and ρ implies that the weakened ferroelectricity should be attributed to the increasing leakage current. Usually, magnetic ion doping will reduce the resistivity of a dielectric material and weaken the ferroelectric performance due to the strengthening of exchange interaction between magnetic ions[46,47]. This behavior is consistent with other multiferroic system, such as Co-doped $BiFeO_3$[46] and Fe-doped $BaTiO_3$[47].

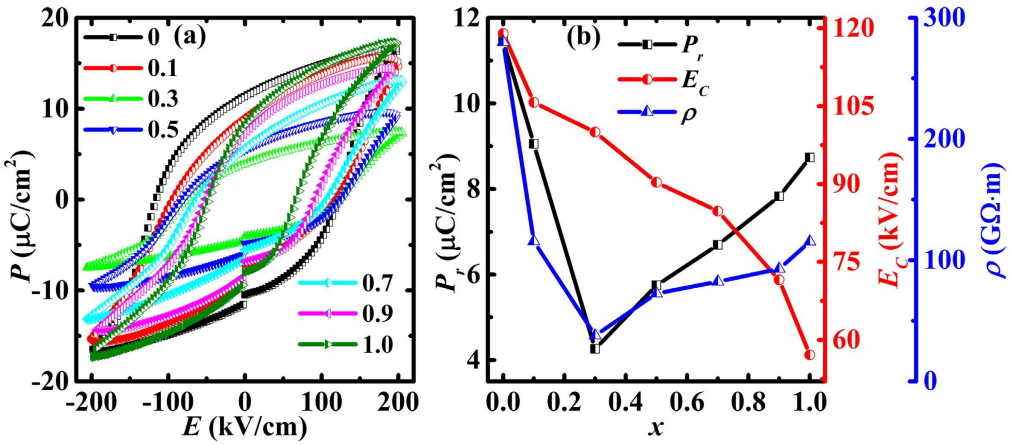

Figure 6. (**a**) Room temperature *P-E* hysteresis loops measured under standard bipolar mode (**b**) P_r, E_c, and ρ *vs. x* curves for BNTFC-*x*.

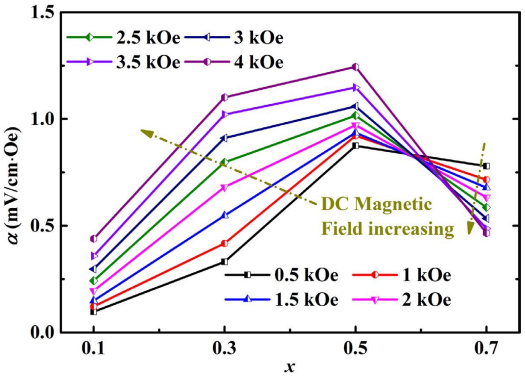

Figure 7. ME coefficients of BNTFC-*x* as a function of cobalt doping level *x*.

The magnetoelectric (ME) effects of the samples with ferromagnetic *M-H* ($x = 0.1$–0.7) are measured at room temperature under an AC magnetic field ~2.27 Oe at 2 kHz, as shown in Fig. 7. The ME coefficients for $x = 0.1$–0.5 gradually increase with the increasing of the applied DC magnetic field, while the ME coefficient for $x > 0.5$ has an opposite behavior, as indicated by the arrows. This difference may be attributed to the different response of the magnetic and electric eigenmodes to the AC magnetic field frequency[48,49]. The largest ME coefficient at room temperature is 1.24 mV/cm·Oe for $x = 0.5$ sample at 4 kOe, comparable with that in 3-layered $Bi_{4-x}Sm_xTi_{3-x}Ni_xO_{12\pm\delta}$ (0.6 mV/cm·Oe)[50], 5-layered $SrBi_5Fe_{0.5}Co_{0.5}Ti_5O_{18}$ ceramic (0.27 mV/cm·Oe at room temperature)[8], cation doped $BiFeO_3$ (0.3–2.3 mV/cm·Oe)[51], and core-shell $50\%CoFe_2O_4$-$50\%BaTiO_3$ (3.4 mV/cm·Oe)[52]. Besides, as mentioned above, some Fe/Co-rich spinel inclusions were observed in the samples. This would lead to the formation of a 0–3 type multiferroic composite, in which another kind of ME coupling effect induced by the magnetostrictive effect from the magnetic phase and the piezoelectric effect from the piezoelectric phase could be obtained[53]. For example, in $xCoFe_2O_4$-$(1-x)Bi_4Ti_3O_{12}$ composite, a much smaller ME coefficient about 0.16 mV/cm·Oe is observed for $x = 0.6$[54]. However, considering the maximal volume fractions of the magnetic inclusions in our samples are smaller than 0.09%, the contribution to the ME coefficient from the inclusions can be neglected[53].

Conclusions

In summary, the 4- and 3-layered intergrowth Aurivillius ceramics $Bi_4NdTi_3Fe_{1-x}Co_xO_{15}$-$Bi_3NdTi_2Fe_{1-x}Co_xO_{12-\delta}$ with a natural superlattice structure were successfully synthesized, offering us a platform to investigate the relationship between the superlattice structure and physical properties *via* conventional methods. By increasing the cobalt doping concentration, the 4-layered parent phase gradually transforms to 3-layered phase, corresponding to a structure evolution. The 4-layered and 3-layered phase can clamp or modulate each other *via* the lattice mismatch. So the observed properties are beyond a simple combined effect of the two phases. As cobalt doping level increases, the ferromagnetism appears in the ferroelectric material, and the remanent magnetization gradually increases and reaches the maximum value at $x = 0.3$, accompanied by the decreasing of remanent ferroelectric polarization. When further increasing the cobalt doping concentration, the remanent magnetization decreases along with the increasing of ferroelectricity. The variation of magnetic and ferroelectric properties can be well explained by the superlattice structure evolution. Furthermore, all samples with ferromagnetic *M-H* ($x = 0.1$–0.7) show ME effect at room temperature, and the largest ME coefficient is in $x = 0.5$ sample.

Methods

The polycrystalline intergrowth superlattice structure $Bi_4NdTi_3Fe_{1-x}Co_xO_{15}$-$Bi_3NdTi_2Fe_{1-x}Co_xO_{12-\delta}$ (BNTFC-x) with $x = 0$, 0.1, 0.3, 0.5, 0.7, 0.9 and 1.0 were prepared by a conventional solid-state reaction method. Note that all the samples were synthesized with 4-layered nominal composition as $Bi_4NdTi_3Fe_{1-x}Co_xO_{15}$. The stoichiometric amounts Bi_2O_3 (with 10 wt. % excess Bi_2O_3 to compensate volatilization loss during the sintering process), Nd_2O_3, Fe_2O_3, Co_2O_3, and TiO_2 powders were mixed by grinding. The mixtures were then pre-sintered at 850 °C for 20 h, and subsequently grounded, pelletized and calcined at 900 °C for 20 h. The obtained samples were cut into the form of pellets with the area of $4 \times 4\,mm^2$. For electrical measurement, the samples were well-polished to thickness of 0.120 mm, and deposited Au electrodes onto the opposite surfaces by sputtering. Due to the extra amount of Bi and the generation of secondary phase, the stoichiometries discussed are nominal (see Supplementary information Table S2 for actual stoichiometry determined by EDS).

Crystalline structures of the samples were characterized by powder X-ray diffraction (XRD) using Cu $K_{\alpha 1}$ radiation (Philips X'Pert Pro diffractometer), and high-angle annular dark-field (HAADF) images (JEOL JEM-2010 field emission electron microscope). Ferroelectric measurement was performed on Radiant Technologies Precision Premier II (Radiant Tech., USA). Magnetic properties were measured using a SQUID-VSM (Quantum Design, USA). The scanning electron microscopy (SEM) images (including secondary-electron (SE) and energy selective backscatter (ESB) images) and EDX were performed on Zeiss Gemini SEM 500 equipped with an ESB detector and an Oxford X-Max 80 detector. The magnetoelectric (ME) voltage coefficient was determined by measuring the electric field generated across the sample with ac magnetic fields (H_{ac} about 2 Oe) and *dc* bias fields (H_{dc} up to 5 kOe), performed on Super M-E system (Quantum Design). A signal generator amplified by a power amplifier was used to drive a Helmholtz coil to generate the small H_{ac} superimposed on H_{dc}. The voltage generated across the sample was measured with a lock-in amplifier. The ME measurement was performed at room temperature.

References

1. Mandal, P. *et al.* Designing switchable polarization and magnetization at room temperature in an oxide. *Nature* **525,** 363–366 (2015).
2. Garcia-Castro, A. C., Romero, A. H. & Bousquet, E. Strain-Engineered Multiferroicity in Pnma $NaMnF_3$ Fluoroperovskite. *Phys. Rev. Lett.* **116,** 117202 (2016).
3. Yadav, A. K. *et al.* Observation of polar vortices in oxide superlattices. *Nature* **530,** 198–201 (2016).
4. Wang, J. *et al.* Epitaxial $BiFeO_3$ Multiferroic Thin Film Heterostructures. *Science* **14,** 1719–1722 (2003).
5. Nakajima, T. *et al.* Uniaxial-stress control of spin-driven ferroelectricity in multiferroic $Ba_2CoGe_2O_7$. *Phys. Rev. Lett.* **114,** 067201 (2015).
6. Aoyama, T. *et al.* Giant spin-driven ferroelectric polarization in $TbMnO_3$ under high pressure. *Nat. Commun.* **5,** 4927 (2014).
7. Zhao, L., Fernández-Díaz, M. T., Tjeng, L. H. & Komarek, A. C. Oxyhalides: A new class of high-T_C multiferroic materials. *Sci. Adv.* **2,** 1600353 (2016).
8. Wang, J. L. *et al.* Low magnetic field response single-phase multiferroics under high temperature. *Mater. Horiz.* **2,** 232–236 (2015).
9. Keeney, L. *et al.* Magnetic Field-Induced Ferroelectric Switching in Multiferroic Aurivillius Phase Thin Films at Room Temperature. *J. Am. Ceram. Soc.* **96,** 2339–2357 (2013).
10. Subbarao, E. C. Crystal Chemistry of Mixed Bismuth Oxides with Layer-Type Structure. *J. Am. Ceram. Soc.* **45,** 166–169 (1962).
11. Newnham, R. E., Wolfe, R. W. & Dorrian, J. F. Structural basis of ferroelectricity in the bismuth titanate family. *Mater. Res. Bull* **6,** 1029–1039 (1971).
12. Ding, Y., Liu, J. S., Qin, H. X., Zhu, J. S. & Wang, Y. N. Why lanthanum-substituted bismuth titanate becomes fatigue free in a ferroelectric capacitor with platinum electrodes. *Appl. Phys. Lett.* **78,** 4175–4177 (2001).
13. Kao, M. C., Chen, H. Z., Young, S. L. & Kao, M. H. Structural, ferroelectric and leakage current properties of $Bi_{3.96}Pr_{0.04}Ti_{2.95}Nb_{0.05}O_{12}$ thin films. *Thin Solid Films* **570,** 543–546 (2014).
14. Wang, J. L. *et al.* Structural Evolution and Multiferroics in Sr-Doped $Bi_7Fe_{1.5}Co_{1.5}Ti_3O_{21}$ Ceramics. *J. Am. Ceram. Soc.* **98,** 1528–1535 (2015).
15. Paul, J., Bhardwaj, S., Sharma, K. K., Kotnala, R. K. & Kumar, R. Room temperature multiferroic properties and magnetoelectric coupling in Sm and Ni substituted $Bi_{4-x}Sm_xTi_{3-x}Ni_xO_{12\pm\delta}$ (x=0, 0.02, 0.05, 0.07) ceramics. *J. Appl. Phys.* **115,** 204909 (2014).
16. Yang, F. J. *et al.* Large magnetic response in $(Bi_4Nd)Ti_3(Fe_{0.5}Co_{0.5})O_{15}$ ceramic at room-temperature. *J. Appl. Phys.* **110,** 126102 (2011).
17. Zhang, D. L. *et al.* Oxygen vacancy-induced ferromagnetism in $Bi_4NdTi_3FeO_{15}$ multiferroic ceramics. *J. Appl. Phys.* **120,** 154105 (2016).
18. Zhang, H., Yan, H. & Reece, M. J. High temperature lead-free relaxor ferroelectric: Intergrowth Aurivillius phase $BaBi_2Nb_2O_9$–$Bi_4Ti_3O_{12}$ ceramics. *J. Appl. Phys.* **107,** 104111 (2010).
19. Zhang, F., Li, Y., Gu, H. & Gao, X. Local orderings in long-range-disordered bismuth-layered intergrowth structure. *J. Solid State Chem.* **212,** 165–170 (2014).
20. Preethi Meher, K. R. S. & Varma, K. B. R. $Bi_4Ti_3O_{12}$–$5BiFeO_3$ Aurivillius intergrowth: Structural and ferroelectric properties. *J. Appl. Phys.* **106,** 124103 (2009).
21. Noguchi, Y., Miyayama, M. & Kudo, T. Ferroelectric properties of intergrowth $Bi_4Ti_3O_{12}$–$SrBi_4Ti_4O_{15}$ ceramics. *Appl. Phys. Lett.* **77,** 3639 (2000).
22. Kobayashi, T., Noguchi, Y. & Miyayama, M. Enhanced spontaneous polarization in superlattice-structured $Bi_4Ti_3O_{12}$–$BaBi_4Ti_4O_{15}$ single crystals. *Appl. Phys. Lett.* **86,** 012907 (2005).
23. Lutterotti, L., Matthies, S. & Wenk, H. MAUD: a friendly Java program for material analysis using diffraction. *Newsletter of the CPD* **21,** 14–15 (1999).
24. Lutterotti, L., Matthies, S. & Wenk, H. MAUD (material analysis using diffraction): a user friendly Java program for Rietveld texture analysis and more. *Proceeding of the twelfth international conference on textures of materials* (*ICOTOM-12*) **1,** 1599 (1999).
25. Hervoches, C. H. *et al.* Structural Behavior of the Four-Layer Aurivillius-Phase Ferroelectrics $SrBi_4Ti_4O_{15}$ and $Bi_5Ti_3FeO_{15}$. *J. Solid State Chem.* **164,** 280–291 (2002).
26. Hervoches, C. H. & Lightfoot, P. A Variable-Temperature Powder Neutron Diffraction Study of Ferroelectric $Bi_4Ti_3O_{12}$. *Chemistry of Materials* **11,** 3359–3364 (1999).
27. Radaev, S. F., Muradyan, L. A. & Simonov, V. I. Atomic Structure and Crystal Chemistry of Sillenites: $Bi_{12}(Bi_{0.5}{}^{3+}Fe_{0.5}{}^{3+})O_{19.5}$ and $Bi_{12}(Bi_{0.67}{}^{3+}Zn_{0.33}{}^{2+})O_{19.33}$. *Acta Crystallographica Setion B* **47,** 1–6 (1991).
28. Zhao, H. *et al.* Large magnetoelectric coupling in magnetically short-range ordered $Bi_5Ti_3FeO_{15}$ film. *Sci. Rep.* **4,** 5255 (2014).
29. Kanamori, J. Theory of the Magnetic Properties of Ferrous and Cobaltous Oxides, I. *Prog. Theor. Phys.* **17,** 177–196 (1957).
30. Kanamori, J. Theory of the Magnetic Properties of Ferrous and Cobaltous Oxides, II. *Prog. Theor. Phys.* **17,** 197–222 (1957).
31. Goodenough, J. B. An interpretation of the magnetic properties of the perovskite-type mixed crystals $La_{1-x}Sr_xCoO_3$. *J. Phys. Chem. Solids* **6,** 287–297 (1958).
32. Kittel, C. *Introduction to Solid State Physics*. 8th edn, 306–308 (John Wiley & Sons, Inc., 2004).

33. Mao, X. Y., Wang, W., Chen, X. B. & Lu, Y. L. Multiferroic properties of layer-structured $Bi_5Fe_{0.5}Co_{0.5}Ti_3O_{15}$ ceramics. *Appl. Phys. Lett.* **95,** 082901 (2009).
34. Birenbaum, A. Y. & Ederer, C. Potentially multiferroic Aurivillius phase $Bi_5FeTi_3O_{15}$: Cation site preference, electric polarization, and magnetic coupling from first principles. *Phys. Rev. B* **90,** 214109 (2014).
35. Kubota, M., Oka, K., Yabuta, H., Miura, K. & Azuma, M. Structure and Magnetic Properties of $BiFe_{1-x}Co_xO_3$ and $Bi_{0.9}Sm_{0.1}Fe_{1-x}Co_xO_3$. *Inorganic Chemistry* **52,** 10698–10704 (2013).
36. Chen, X. *et al*. Room temperature magnetoelectric coupling study in multiferroic $Bi_4NdTi_3Fe_{0.7}Ni_{0.3}O_{15}$ prepared by a multicalcination procedure. *Ceram. Int.* **40,** 6815–6819 (2014).
37. Palizdar, M. *et al.* Crystallographic and magnetic identification of secondary phase in orientated $Bi_5Fe_{0.5}Co_{0.5}Ti_3O_{15}$ ceramics. *J. Appl. Phys.* **112,** 073919 (2012).
38. Schmidt, M. *et al.* Absence of evidence not equal evidence of absence: statistical analysis of inclusions in multiferroic thin films. *Sci. Rep*. **4,** 5712 (2014).
39. Goya, G. F., Berqúo, T. S., Fonseca, F. C. & Morales, M. P. Static and dynamic magnetic properties of spherical magnetite nanoparticles. *J. Appl. Phys.* **94,** 3520 (2003).
40. Guan, N., Wang, Y., Sun, D. & Xu, J. A simple one-pot synthesis of single-crystalline magnetite hollow spheres from a single iron precursor. *Nanotechnology* **20,** 105603 (2009).
41. El-Dek, S. I. Effect of annealing temperature on the magnetic properties of $CoFe_2O_4$ nanoparticles. *Philosophical Magazine Letters* **90,** 233–240 (2010).
42. Muthuselvam, I. P. & Bhowmik, R. N. Structural phase stability and magnetism in Co_2FeO_4 spinel oxide. *Solid State Sciences* **11,** 719–725 (2009).
43. Panda, M. R., Bhowmik, R. N., Singh, H., Singh, M. N. & Sinha, A. K. Air annealing effects on lattice structure, charge state distribution of cations, and room temperature ferrimagnetism in the ferrite composition $Co_{2.25}Fe_{0.75}O_4$. *Materials Research Express* **2,** 036101 (2015).
44. Kim, K. J., Lee, J. H. & Kim, C. S. Phase decomposition and related structural and magnetic properties of iron-cobaltite thin films. *Journal of the Korean Physical Society* **61,** 1274–1278 (2012).
45. He, L., Chen, C., Wang, N., Zhou, W. & Guo, L. Finite size effect on Néel temperature with Co_3O_4 nanoparticles. *J. Appl. Phys*. **102,** 103911 (2007).
46. Xi, X. J. *et al.* Enhanced magnetic and conductive properties of Ba and Co co-doped $BiFeO_3$ ceramics. *J. Magn. Magn. Mater.* **355,** 259–264 (2014).
47. Wei, X. K. *et al.* Structure, electrical and magnetic property investigations on dense Fe-doped hexagonal $BaTiO_3$. *J. Appl. Phys.* **110,** 114112 (2011).
48. Tilley, D. R. & Scott, J. F. Frequency dependence of magnetoelectric phenomena in $BaMnF_4$. *Phys. Rev. B* **25,** 3251–3260 (1982).
49. Fiebig, M. Revival of the magnetoelectric effect. *J. Phys. D: Appl. Phys.* **38,** R123–R152 (2005).
50. Paul, J., Bhardwaj, S., Sharma, K. K., Kotnala, R. K. & Kumar, R. Room-temperature multiferroic properties and magnetoelectric coupling in $Bi_{4-x}Sm_xTi_{3-x}Co_xO_{12-\delta}$ ceramics. *J. Mater. Sci.* **49,** 6056–6066 (2014).
51. Naik, V. B. & Mahendiran, R. Magnetic and magnetoelectric studies in pure and cation doped $BiFeO_3$. *Solid State Commun*. **149,** 754–758 (2009).
52. Grössinger, R., Duong, G. V. & Sato-Turtelli, R. The physics of magnetoelectric composites. *J. Magn. Magn. Mater.* **320,** 1972–1977 (2008).
53. Nan, C.-W., Bichurin, M. I., Dong, S., Viehland, D. & Srinivasan, G. Multiferroic magnetoelectric composites: Historical perspective, status, and future directions. *J. Appl. Phys.* **103,** 031101 (2008).
54. Suryanarayana, S. V. Magnetoelectric interaction phenomena in materials. *Bulletin of Materials Science* **17,** 1259–1270 (1994).

Acknowledgements

This work is supported by the National Natural Science Foundation of China, and the National Basic Research Program of China (2016YFA0300103, 2015CB921201 and 2012CB922003). This work was partially carried out at the USTC Center for Micro and Nanoscale Research and Fabrication. The authors also thank Drs. S. Q. Fu, J. L. Huang, and Y. Lin at the USTC Instruments' Center for Physical Science for the SEM and TEM measurements.

Author Contributions

X.G.L. and Y.W.Y. designed and supervised the experiments; D.L.Z. and Z.W.C. prepared the sample; D.L.Z., W.C. H. and S.N.D carried out HAADF and SAED measurements and assisted in analyzing the relative data; D.L.Z., W.C. H and L.F. performed the XRD measurements and Rietveld refinements; D.L.Z., W.B.Z and L.F characterized the ferroelectric and magnetic properties; M.L. performed the SEM and EDX measurements; D.L.Z., X.G.L. and Y.W.Y. were responsible for all data analysis and wrote the manuscript. All authors contributed to the discussions and editing of the manuscript.

Additional Information

Supplementary information accompanies this paper at http://www.nature.com/srep

Competing financial interests: The authors declare no competing financial interests.

How to cite this article: Zhang, D. L. *et al.* Structure Evolution and Multiferroic Properties in Cobalt Doped $Bi_4NdTi_3Fe_{1-x}Co_xO_{15}$-$Bi_3NdTi_2Fe_{1-x}Co_xO_{12-\delta}$ Intergrowth Aurivillius Compounds. *Sci. Rep.* **7**, 43540; doi: 10.1038/srep43540 (2017).

Publisher's note: Springer Nature remains neutral with regard to jurisdictional claims in published maps and institutional affiliations.

Supplementary material

Structure Evolution and Multiferroic Properties in Cobalt Doped $Bi_4NdTi_3Fe_{1-x}Co_xO_{15}$-$Bi_3NdTi_2Fe_{1-x}Co_xO_{12-\delta}$ Intergrowth Aurivillius Compounds

D. L. Zhang,[1] W. C. Huang,[1] Z. W Chen,[1] W. B. Zhao,[1] L. Feng,[1] M. Li,[1] Y. W. Yin,[1, 2, a)] S. N. Dong,[1] X. G. Li[1, 3, 4, a)]

[1]*Hefei National Laboratory for Physical Sciences at the Microscale, Department of Physics, University of Science and Technology of China, Hefei 230026, China*

[2]*Department of Physics and Astronomy, University of Nebraska, Lincoln, NE 68588, USA*

[3]*Key Laboratory of Materials Physics, Institute of Solid State Physics, CAS, Hefei 230026, China*

[4]*Collaborative Innovation Center of Advanced Microstructures, Nanjing 210093, China*

I. Statistical analysis of second phase magnetic inclusions: volume fractions and magnetic contributions

In previous researches, M. Palizdar *et al.*,[1] L. Keeney *et al*.[2] and M. Schmidt *et al*.[3] provided an original methodology for the detection, localization and quantification of second phase inclusions in Aurivillius phase *via* energy selective backscatter (ESB) image and energy dispersive X-ray analysis (EDX). The backscatter electron is sensitive to the mean atomic number,[4] therefore it is one of the ideal techniques for searching for possible secondary phases. In an ESB image, high atomic number regions appear bright, while low atomic number regions appear dark.[1] To determine the magnetic contribution from the ferromagnetic secondary inclusions, the scanning electron microscopy (SEM) images (including secondary-electron (SE) images and ESB images) and EDX were performed for all $Bi_4NdTi_3Fe_{1-x}Co_xO_{15}$-$Bi_3NdTi_2Fe_{1-x}Co_xO_{12-\delta}$ (BNTFC-*x*, *x* = 0.0, 0.1, 0.3, 0.5, 0.7, 0.9, and 1.0) samples on Zeiss Gemini SEM 500 equipped with an ESB detector and an Oxford X-Max 80 detector.

Taking *x* = 0.3 sample as an example, Fig. S1 shows the ESB image and corresponding Bi, Co and Fe intensity maps (acquired from the EDX mapping). The circled region (with black contrast in Fig. S1 (a)) are Co and Fe rich (Bi poor) areas,

a) Author to whom correspondence should be addressed. Electronic mail: lixg@ustc.edu.cn and yyin11@unl.edu

demonstrating the existence and location of the Fe and Co-rich secondary phase.[1]

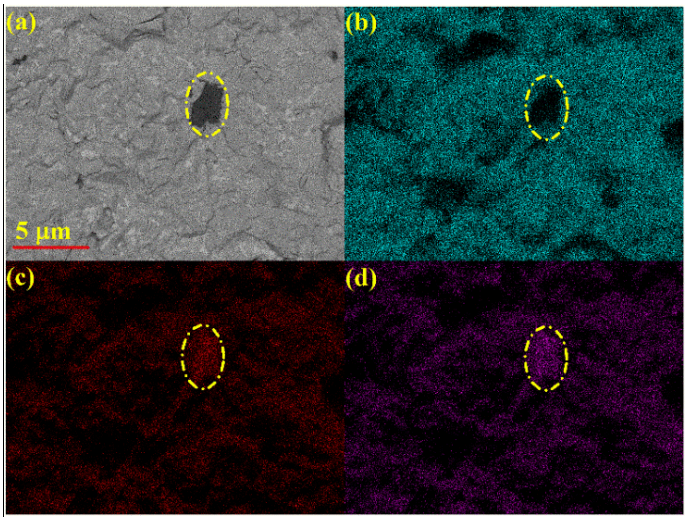

Fig. S1. (a) ESB image and corresponding (b) Bi, (c) Fe and (d) Co intensity map for x = 0.3 sample. The inclusions are marked by a circle.

Figs. S2 (a) and (b) show the SE image and corresponding ESB image of x = 0 sample on a relatively large area (10^4 μm^2). Comparing the two images, all dark regions in the ESB image of Fig. S2 (b) are related to the pores or grain boundaries. The ESB image together with the EDX mapping was acquired on a smaller area (25 μm^2) to further verify whether there exist Fe-rich regions, as shown in Figs. S2 (c) and (d). The Fe K intensity map shows no obvious Fe-rich region, probably indicating that no Fe-rich secondary phase was formed in x = 0 sample.

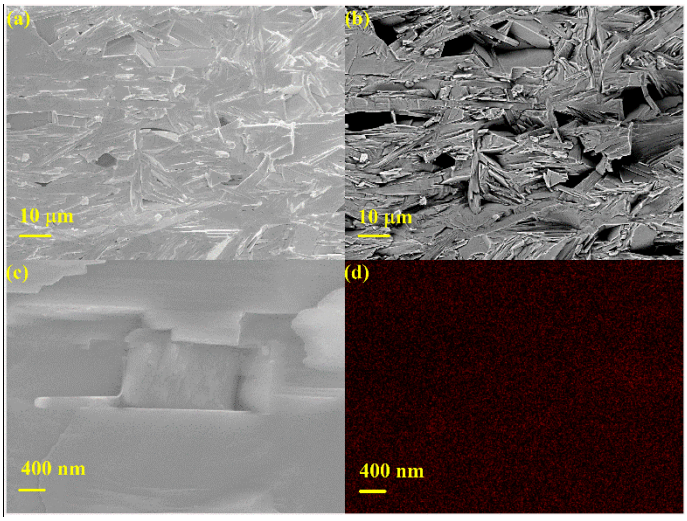

Fig. S2. (a) SE image and (b) corresponding ESB image of x = 0 sample on an area of 10^4 μm^2; (c) ESB image and (d) Fe K intensity map for x = 0 on an area of 25 μm^2.

For x = 0.1 - 1.0, series measurements with different scanning area sizes and different minimal detectable grain dimensions, were made to estimate the volume fraction of the inclusions, as shown in Figs. S3-S8.The mean atomic number Z_m of the three phases, $Bi_{12}TiO_{20}$, BNTFC-x, and $Fe_{3-y}Co_yO_4$ ($0 \leq y \leq 3$), have a relationship of Z_m=35.7 ($Bi_{12}TiO_{20}$) > 25.1-25.5 (NTFC-x) > 15.7-16.1 ($Fe_{3-y}Co_yO_4$), and therefore in ESB images, $Bi_{12}TiO_{20}$ phase should be brighter and $Fe_{3-y}Co_yO_4$ inclusions should be darker. Take x=0.5 in Fig. S5 for example, the black regions (such as the black area marked by a red circle) represent the Fe/Co rich spinel magnetic inclusion phase. While the gray regions, which have the largest area, denote the main phase. In addition, as discussed in the main text, with increasing the Co doping level x, an impurity phase $Bi_{12}TiO_{20}$ with higher Bi composition appears, which is the brightest in the ESB images (*e.g.* the white area marked by a blue circle). These are also supported by the local EDS measurements (see following discussion). For x = 0.1 - 1.0, representative areas for the magnetic inclusions (black in ESB image) and $Bi_{12}TiO_{20}$ phase (white in ESB image) are marked out representatively by red and blue circles in Figs. S3-S8.

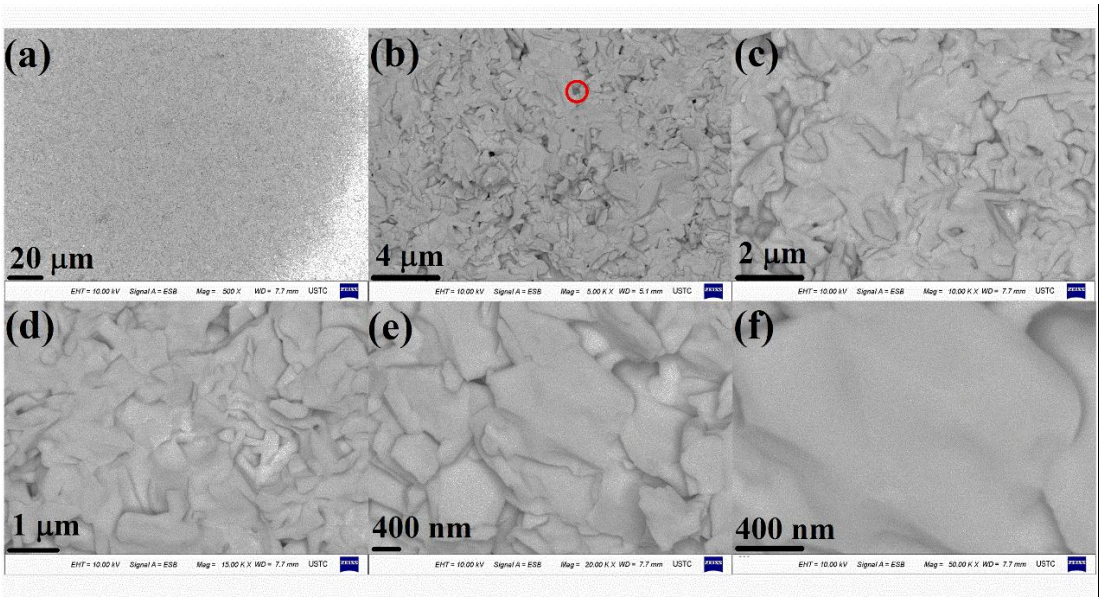

Fig. S3. ESB images for x = 0.1 sample with different scan area sizes, (a) 40000 μm^2, (b) 400 μm^2, (c) 100 μm^2, (d) 44.4 μm^2, (e) 25 μm^2, and (f) 4 μm^2. The bright circle at the corner of (a) is due to the 500× magnification factor approach the limit of the reception range of the ESB detector. A black inclusion in (b) marked by a red circle is a representative Fe/Co rich spinel phase.

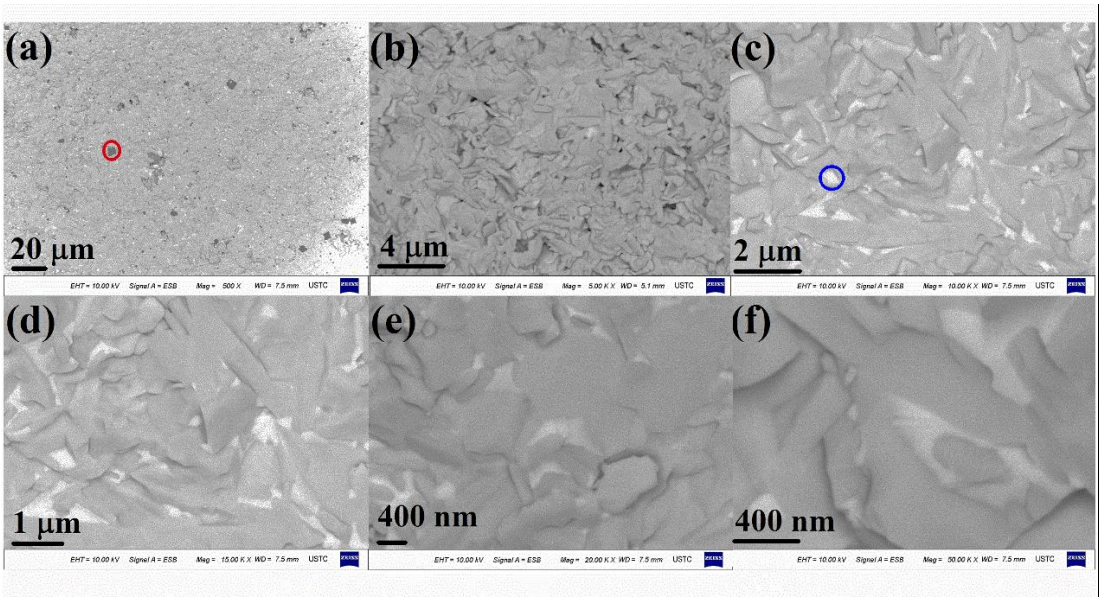

Fig. S4. ESB images for x = 0.3 sample in different magnification factors, (a) 40000 μm^2, (b) 400 μm^2, (c) 100 μm^2, (d) 44.4 μm^2, (e) 25 μm^2, and (f) 4 μm^2. A black inclusion in (a) marked by a red circle is a representative Fe/Co rich spinel phase, and a white one in (c) marked by a blue circle is $Bi_{12}TiO_{20}$

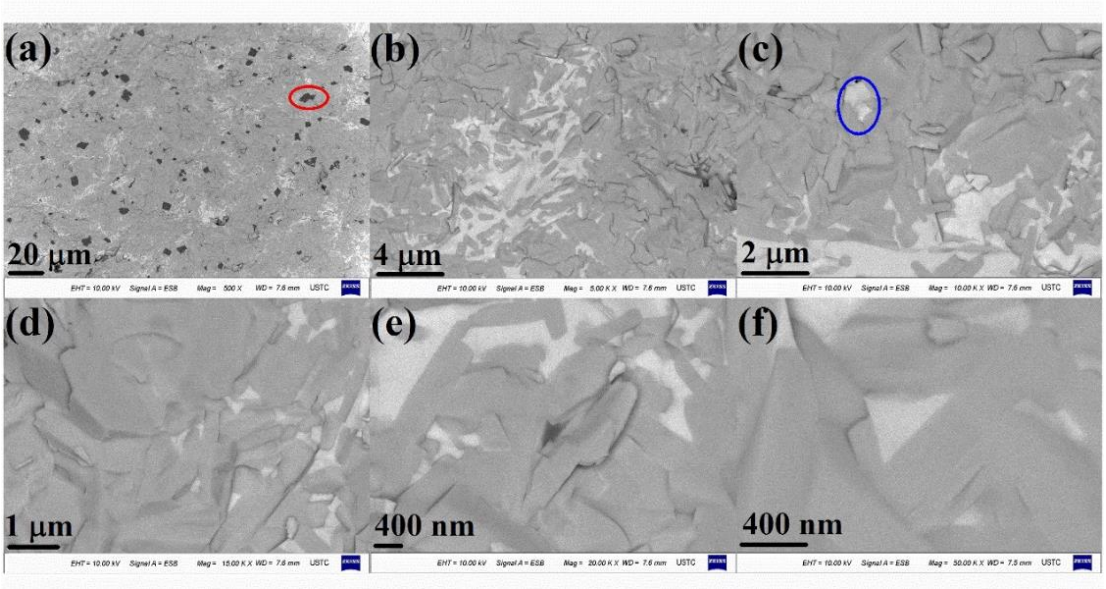

Fig. S5. ESB images for x = 0.5 sample in different magnification factors, (a) 40000 μm^2, (b) 400 μm^2, (c) 100 μm^2, (d) 44.4 μm^2, (e) 25 μm^2, and (f) 4 μm^2. A black inclusion in (a) marked by a red circle is Fe/Co rich spinel phase, and a white one in (c) marked by a blue circle is $Bi_{12}TiO_{20}$.

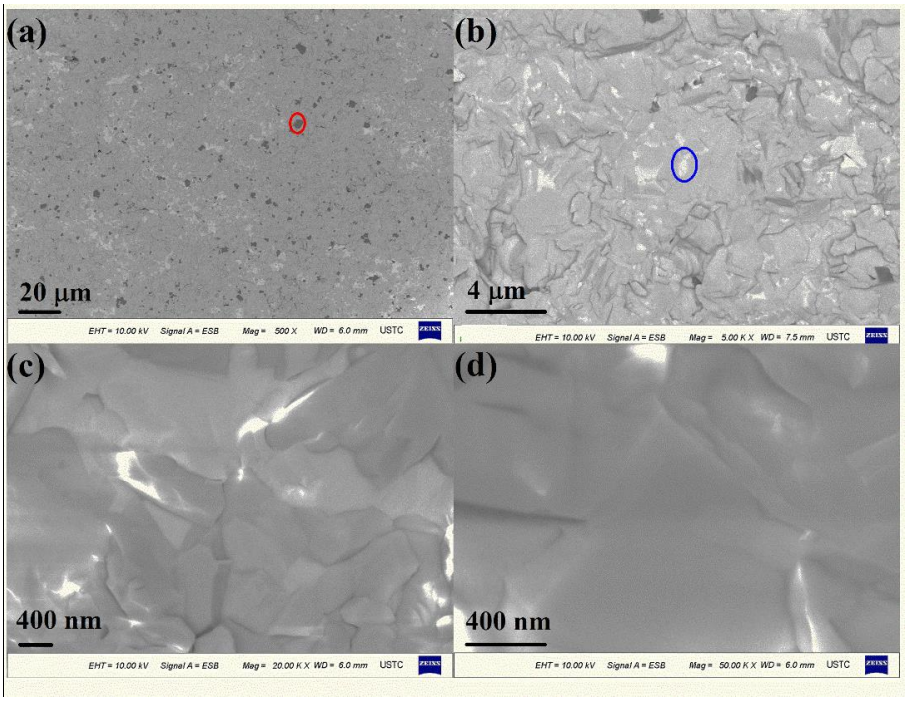

Fig. S6. ESB images for x = 0.7 sample in different magnification factors, (a) 40000 μm^2, (b) 400 μm^2, (c) 25 μm^2, and (d) 4 μm^2. A black inclusion in (a) marked by a red circle is Fe/Co rich spinel phase, and a white one in (b) marked by a blue circle is $Bi_{12}TiO_{20}$.

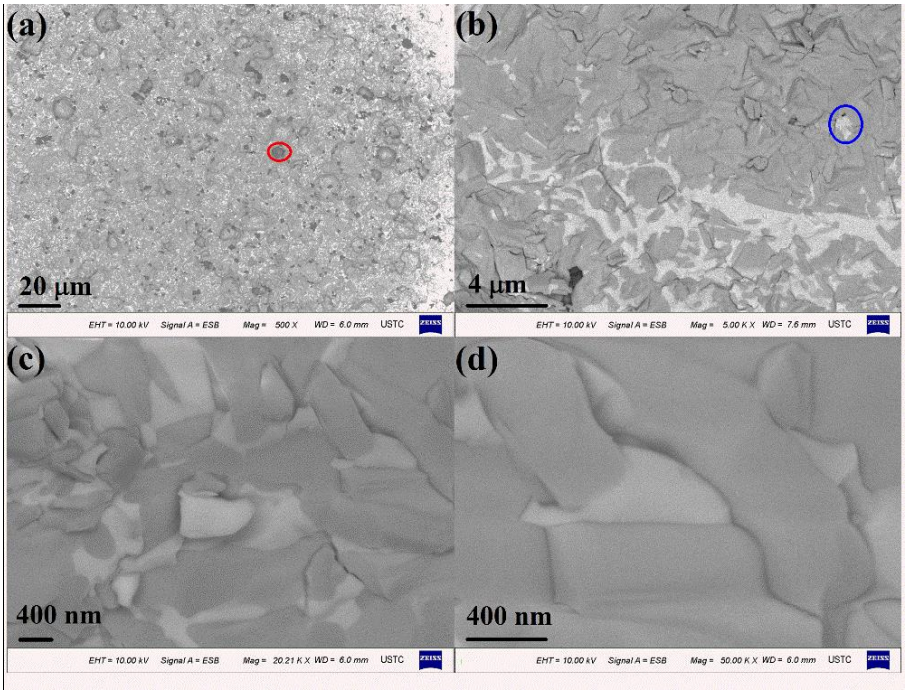

Fig. S7. ESB images for x = 0.9 sample in different magnification factors, (a) 40000 μm^2, (b) 400 μm^2, (c) 25 μm^2, and (d) 4 μm^2. A black inclusion in (a) marked by a red circle is Fe/Co rich spinel phase, and a white one in (b) marked by a blue circle is $Bi_{12}TiO_{20}$.

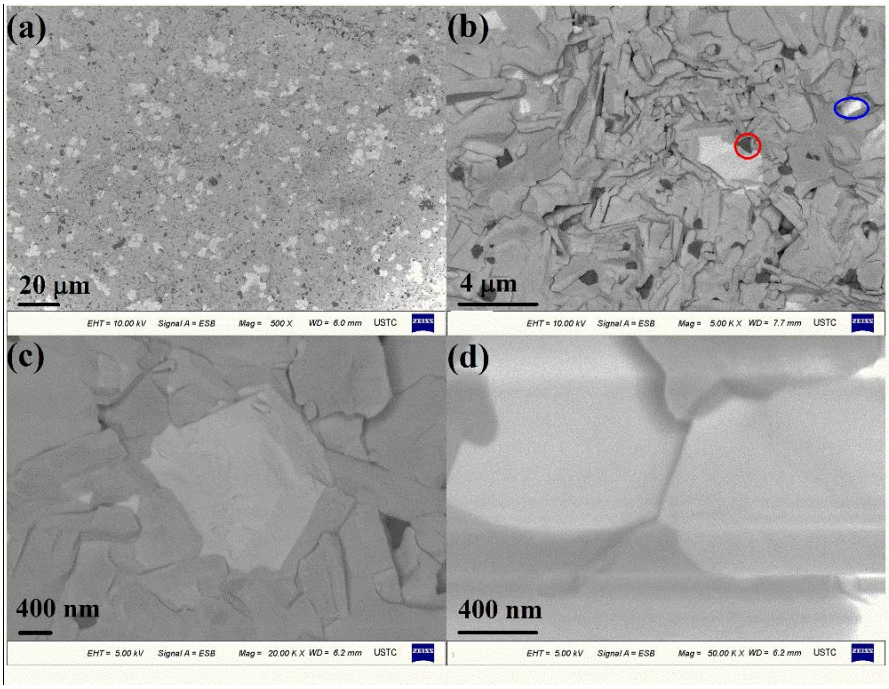

Fig. S8. ESB images for x = 1.0 sample in different magnification factors, (a) 40000 μm^2, (b) 400 μm^2, (c) 25 μm^2, (d) and 4 μm^2. A black inclusion in (b) marked by a red circle is Fe/Co rich spinel phase, and a white one marked by a blue circle is $Bi_{12}TiO_{20}$.

Generally, the Fe and Co-rich magnetic inclusions have a chemical formula $Fe_{3-y}Co_yO_4$ ($0 \le y \le 3$), and its remanent magnetization at room temperature decreases as Co content increases.[5-10] In order to give a reasonable estimation of the magnetic contribution from the inclusions, the chemical compositions of the inclusions for all samples were calculated from the EDX mapping. The mole ratios of Fe/Co (Δ) in the inclusions can be obtained by analyzing the inclusion intensities of the EDX mapping.

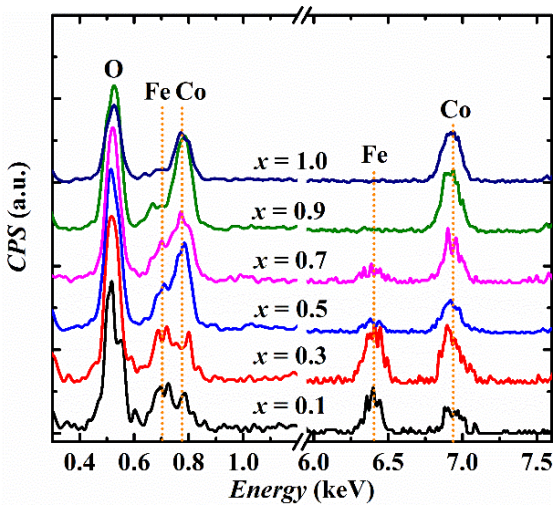

Fig. S9. Energy dispersive X-ray spectrometry (EDS) of the inclusions for x = 0.1-1.0 samples.

Fig. S9 shows the EDS (energy dispersive X-ray spectrometry) of the inclusions for x = 0.1-1.0 samples. It can be clearly seen that the intensity ratio of Fe/Co gradually decreases with increasing Co concentration. Based on the chemical formula of the magnetic inclusions $Fe_{3-y}Co_yO_4$ ($0 \le y \le 3$)[3,5-10], the chemical compositions can be calculated by $y = 3/(1+\Delta)$. For x = 0.1 and 0.3, the Fe/Co mole ratios (Δ) of the inclusions are determined to be 1.17±0.25 and 0.91±0.24, respectively. Thus the inclusions would be $Fe_{1.61}Co_{1.39}O_4$ and $Fe_{1.43}Co_{1.57}O_4$ respectively, and M_{Ir} (the remanent magnetization of the inclusions) could be set to 17 emu/g (the worst case scenario is Fe_2CoO_4 (13-17 emu/g)[7]). For x = 0.5, the Fe/Co mole ratio of the inclusions is 0.37±0.18, indicating the inclusions may be Co-rich spinel phases $Fe_{0.8}Co_{2.2}O_4$ having M_{Ir} of 5.5 emu/g.[10] For x = 0.7, the Fe/Co mole ratio of the inclusions is 0.17±0.12, and the chemical formula for the inclusions would be $Fe_{0.44}Co_{2.56}O_4$ with M_{Ir} of 0.73 emu/g ($Fe_{0.5}Co_{2.5}O_4$).[10] For x = 0.9 and 1.0, the Fe/Co mole ratios of the inclusions are determined to be 0. Thus the inclusions should be Co_3O_4, which is paramagnetic at 300K,[10,11] and the M_{Ir} could be set to 0 emu/g at 300K. Besides, the Bi/Ti mole ratio of the white region calculated from a point EDS (Fig. S10) is about 11.7/1, confirming that the white regions represent $Bi_{12}TiO_{20}$ phase.

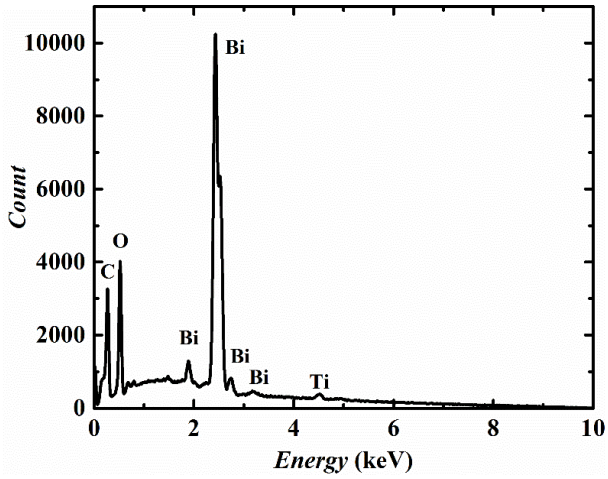

Fig. S10. Energy dispersive X-ray spectrometry (EDS) preformed focus on a white area.

In addition, it is also worth mentioning that the ESB images were acquired at a set resolution of 1024×768 pixels. If the smallest detectable size of inclusions across all scanned areas is defined as 2×2 pixels, which can be distinguished easily, the minimal detectable diameters for scanning areas of 40000 μm^2 (largest scan area) and 4 μm^2 (smallest scan area) are 450 nm and 4.5 nm, respectively. The ferromagnetic

contributions from Fe_3O_4[5,12] and $CoFe_2O_4$[13] inclusions with grain sizes smaller than 5 nm, having a blocking temperature below 300 K, could be neglected at 300 K. In our case, no Fe/Co rich area with a size smaller than 200 nm was observed for all samples. This may be attributed to the high synthesis temperature and long sintering time (pre-sintered at 850 °C for 20 h and calcined at 900 °C for 20 h), which would make the grain size of inclusions grow large.[14]

Assuming that all inclusions are spherical, and following the statistical method proposed by M. Schmidt *et al*.[3], the upper limit of volume fraction $f_{k,u}$ for the inclusions with the sizes between d_k and d_{k-1} ($d_{k-1}>d_k$) can be calculated by

$$f_{k,u} \approx 2.8\frac{d_{k-1}^3}{\sum_{j=K}^{k} V_j} \tag{1}$$

with a confidence of $\gamma = 99.5\%$, and V_j is an individual scan of a series scans ($k = 1, \ldots, K$).

In order to apply the statistical method to the ESB or EDX images of our samples, formula (1) can be modified to 2-dimension model as follow:

$$f_{k,u,s} \approx 4.16\frac{d_{k-1}^2}{\sum_{j=K}^{k} S_j} \tag{2}$$

In an isotropic ceramic system, it is reasonable to assume that the inclusions evenly distribute in the samples, thus the volume fraction f_V of the inclusions can be obtained from f_s by

$$f_V = (\sqrt{f_s})^3 \tag{3}$$

Therefore, the volume fraction of the inclusions can be calculated from the ESB images by using equations (1)-(3). Although the size of the inclusions in our samples is larger than 200 nm, the scans with minimal detectable diameter smaller than 200 nm were also performed for statistical analysis. The detailed results are listed in Table S1.

Given the volume fraction of the ferromagnetic inclusions, the maximal contribution from the inclusions (M_i) with diameter between [d_k, d_{k-1}] can be calculated by:

$$M_{i,k} = f_{m,k}M_{Ir,k} = \frac{f_{V,k}\rho_i}{f_{V,k}\rho_i + f_{V,main}\rho_{main} + f_{V,\text{sillenite}}\rho_{\text{sillenite}}}M_{Ir,k} \tag{4}$$

where $M_{Ir,k}$ is the remanent magnetization of the inclusions, $f_{m,k}$ is the mass fraction of the inclusions, $f_{V,main}$ and ρ_{main} are the volume fraction and density of the main phase respectively, $f_{V,sillenite}$ and $\rho_{\text{sillenite}}$ are the volume fraction and density of sillenite

$Bi_{12}TiO_{20}$ respectively. Thus the magnetization remanence from the inclusions has an up bound

$$M_i = \max_{k=1...K}\{M_{i,k}\} \tag{5}$$

with a confidence γ = 99.5%.

Table S1. Performed scans for x = 0.1-1.0 samples. M_r is the remanent magnetization of x = 0.1-1.0 samples, and d_0 is the maximum size of inclusions found in the sample.

x	M_r (memu/g)	Fe/Co ratio	k	Area (μm^2)	d_k (nm)	f_V (%)	M_i (memu/g)
0.1	17.3	1.17 (±0.25)	1	40000	450 (d_0=2.86μm)	2.4E-3	0.29
			2	400	45	5.6E-3	0.67
			3	100	22.5	3.4E-5	0.004
			4	44.4	15	1.5E-5	0.002
			5	25	11.25	1.8E-5	0.002
			6	4	4.5	1.5E-4	0.018
0.3	123	0.91 (±0.24)	1	40000	450 (d_0=5.71μm)	1.9E-2	2.31
			2	400	45	5.6E-3	0.67
			3	100	22.5	3.4E-5	0.004
			4	44.4	15	1.5E-5	0.002
			5	25	11.25	1.8E-5	0.002
			6	4	4.5	1.5E-4	0.018
0.5	89.9	0.37 (±0.18)	1	40000	450 (d_0=9.5μm)	9.0E-2	3.31
			2	400	45	5.6E-3	0.21
			3	100	22.5	3.4E-5	0.0012
			4	44.4	15	1.5E-5	0.0006
			5	25	11.25	1.8E-5	0.0007
			6	4	4.5	1.5E-4	0.006
0.7	7.02	0.17 (±0.12)	1	40000	450 (d_0=5.71μm)	2.0E-2	0.11
			2	400	45	8.7E-3	0.05
			3	25	11.25	5.0E-4	0.0026
			4	4	4.5	1.5E-4	0.0008
0.9	0.026	0	1	40000	450 (d_0=6.67μm)	3.1E-2	0
			2	400	45	8.7E-3	0
			3	25	11.25	5.0E-4	0
			4	4	4.5	1.5E-4	0
1.0	0.022	0	1	40000	450 (d_0=7.62μm)	4.6E-2	0
			2	400	45	8.7E-3	0
			3	25	11.25	5.0E-4	0
			4	4	4.5	1.5E-4	0

According to the above analysis, the upper limit impact on magnetic contributions to M_r from the inclusions (M_i) for x = 0.1, 0.3, 0.5, 0.7, 0.9 and 1.0 are 0.67 memu/g, 2.31 memu/g, 3.31 memu/g, 0.11 memu/g, 0 and 0, respectively, as listed in Table S1. It is found that the magnetic contributions of the inclusions are much smaller than the total magnetizations measured for all samples. For the samples with ferromagnetic signals, namely, x = 0.1, 0.3, 0.5, and 0.7, the magnetic contributions to the corresponding main phases of the inclusions are conservatively estimated to be about or smaller than 3.9%, 1.9%, 3.8%, and 1.5%, respectively. Following the criteria of the comprehensive framework raised by M. Schmidt *et al*.[3], this indicates that the magnetic results do represent intrinsic information of the main phase.

II. Actual stoichiometry from EDX analysis for $Bi_4NdTi_3Fe_{1-x}Co_xO_{15}$-$Bi_3NdTi_2Fe_{1-x}Co_xO_{12-\delta}$ (x = 0.0, 0.1, 0.3, 0.5, 0.7, 0.9, and 1.0) samples

The actual stoichiometries (mole ratio, normalized by Ti element) of the samples determined by energy dispersive X-ray analysis (EDX) mapping are listed in Table S2. The mole ratios of Bi, Nd and Ti change little, while those of Fe, Co vary with the nominal doping level. The volume fractions for 4- and 3-layered phases and $Bi_{12}TiO_{20}$ listed in Table S2 are modified by calculating the franction of magnetic inclusions, thus these values have a small difference with those obtained by XRD refinements.

Table S2. The volume fractions and chemical constituents of the samples (normalized by Ti element)

x	Volume Fraction (%)				Bi	Nd	Ti	Fe	Co
	4-layer	3-layer	$Bi_{12}TiO_{20}$	Inclusions*					
0	100	0	0	0	1.35	0.28	1	0.30	-
0.1	99.99	0	0	5.6E-3	1.26	0.37	1	0.28	0.05
0.3	80.09	17.15	2.74	1.9E-2	1.20	0.28	1	0.20	0.10
0.5	42.71	41.71	15.49	9.0E-2	1.20	0.26	1	0.15	0.19
0.7	8.87	77.41	13.70	2.0E-2	1.25	0.28	1	0.08	0.21
0.9	0.29	83.07	16.60	3.1E-2	1.35	0.26	1	0.03	0.27
1.0	0	85.30	14.65	4.6E-2	1.23	0.29	1	-	0.31

* Data from Table S1.

References:

1 Palizdar, M. *et al.* Crystallographic and magnetic identification of secondary phase in orientated $Bi_5Fe_{0.5}Co_{0.5}Ti_3O_{15}$ ceramics. *J. Appl. Phys.* **112**, 073919 (2012).

2 Keeney, L. *et al.* Magnetic Field-Induced Ferroelectric Switching in Multiferroic Aurivillius Phase Thin Films at Room Temperature. *J. Am. Ceram. Soc.* **96**, 2339-2357 (2013).

3 Schmidt, M. *et al.* Absence of evidence not equal evidence of absence: statistical analysis of inclusions in multiferroic thin films. *Sci. Rep.* **4**, 5712 (2014).

4 Itakura, M., Kuwano, N., Sato, K. & Tachibana, S. Variations in contrast of scanning electron microscope images for microstructure analysis of Si-based semiconductor materials. *J Electron Microsc (Tokyo)* **59 Suppl 1**, S165-173 (2010).

5 Goya, G. F., Berquó, T. S., Fonseca, F. C. & Morales, M. P. Static and dynamic magnetic properties of spherical magnetite nanoparticles. *J. Appl. Phys.* **94**, 3520 (2003).

6 Guan, N., Wang, Y., Sun, D. & Xu, J. A simple one-pot synthesis of single-crystalline magnetite hollow spheres from a single iron precursor. *Nanotechnology* **20**, 105603 (2009).

7 El-Dek, S. I. Effect of annealing temperature on the magnetic properties of $CoFe_2O_4$ nanoparticles. *Philosophical Magazine Letters* **90**, 233-240 (2010).

8 Muthuselvam, I. P. & Bhowmik, R. N. Structural phase stability and magnetism in Co_2FeO_4 spinel oxide. *Solid State Sciences* **11**, 719-725 (2009).

9 Panda, M. R., Bhowmik, R. N., Singh, H., Singh, M. N. & Sinha, A. K. Air annealing effects on lattice structure, charge state distribution of cations, and room temperature ferrimagnetism in the ferrite composition $Co_{2.25}Fe_{0.75}O_4$. *Materials Research Express* **2**, 036101 (2015).

10 Kim, K. J., Lee, J. H. & Kim, C. S. Phase decomposition and related structural and magnetic properties of iron-cobaltite thin films. *Journal of the Korean Physical Society* **61**, 1274-1278 (2012).

11 He, L., Chen, C., Wang, N., Zhou, W. & Guo, L. Finite size effect on Néel temperature with Co_3O_4 nanoparticles. *J. Appl. Phys.* **102**, 103911 (2007).

12 Roca, A. G., Morales, M. P., O'Grady, K. & Serna, C. J. Structural and magnetic properties of uniform magnetite nanoparticles prepared by high temperature decomposition of organic precursors. *Nanotechnology* **17**, 2783-2788 (2006).

13 Liu, C., Zou, B., Rondinone, A. J. & Zhang, Z. J. Chemical Control of Superparamagnetic Properties of Magnesium and Cobalt Spinel Ferrite Nanoparticles through Atomic Level Magnetic Couplings. *J. Am. Chem. Soc.* **122**, 6263-6267 (2000).

14 Sedlacik, M., Pavlinek, V., Peer, P. & Filip, P. Tailoring the magnetic properties and magnetorheological behavior of spinel nanocrystalline cobalt ferrite by varying annealing temperature. *Dalton Trans* **43**, 6919-6924 (2014).